ACTA IMEKO
ISSN: 2221-870X
September 2026, Volume 15, Number 3, 1 - 8

Detection of induction motor faults by envelopes of higher current harmonics

Alexander Shestakov[1], Dmitry Galyshev[1], Victoria Eremeeva[1], Vladimir Sinitsin[1], Olga Ibryaeva[1]

[1] *South Ural State University (National Research University), 76 Lenin Avenue, 454080 Chelyabinsk, Russian Federation*

ABSTRACT
Detection of broken rotor bars in induction motors based on sideband components near the fundamental stator current frequency often yields unreliable results under variable operating conditions due to masking effects and the dominant amplitude of the fundamental component. This study proposes a robust fault detection method which uses higher-order current harmonics, which demonstrate significantly reduced susceptibility to load variations and other masking phenomena. As principal contribution this study demonstrates that a convolutional neural network trained exclusively on data derived from a single operating condition achieves strong generalisation across a wide spectrum of unsteady operating regimes, spanning substantially different supply frequencies and load levels, with consistently high classification accuracy. Signal processing involves bandpass filtering around the fifth and seventh harmonic frequencies, envelope extraction via the Hilbert transform, continuous wavelet transform to generate time-frequency scalograms, and data augmentation through vertical shifts to simulate variations in defect-related frequency components under changing slip conditions. Scalograms corresponding to the fifth and seventh harmonics are treated as independent training samples, effectively expanding the dataset while leveraging physically redundant fault information. This single-point training paradigm directly addresses a critical industrial limitation, thereby enabling deployment of data-driven condition monitoring systems even under severe training data constraints.

Section: RESEARCH PAPER

Keywords: induction motor; broken rotor bar; current signal analysis; continuous wavelet transform (CWT); convolutional neural network (CNN)

Citation: A. Shestakov, D. Galyshev, V. Eremeeva, V. Sinitsin, O. Ibryaeva, Detection of induction motor faults by envelopes of higher current harmonics, Acta IMEKO, vol. 15 (2026) no. 3, pp. 1-8. DOI: 10.21014/actaimeko.v15i3.1901

Section Editor: Jakub Svatos, CVUT Prague, Czech Republic

Received July 3, 2024; **In final form** June 23, 2026; **Published** September 2026

Corresponding author: Olga Ibryaeva, e-mail: ibriaevaol@susu.ru

1. INTRODUCTION

Broken bars of squirrel-cage rotors are up to 10 % of all induction motor faults [1]. However, it is important to promptly detect broken bars, since operating a motor with this malfunction leads to an increase in power consumption and a decrease in the operating torque of the motor [2]. A broken bar can also lead to secondary motor failures. For example, a broken rotor bar always causes increased vibration, which leads to rapid wear of the rotor support bearings. Also, the protruding end of a broken bar can lead to jamming of the rotor and damage to the stator winding when the motor is running.

Existing diagnostic methods are based on searching for a defect harmonic (broken bars) in the stator current, equal to $f_{\mathrm{BB}} = 2\,s\,f_{\mathrm{s}}$, where f_{s} is the frequency of the stator current, and s is the motor slip. This harmonic modulates the sinusoidal stator current and creates side peaks in the amplitude spectrum of the current [3] at frequencies:

$$f_{\mathrm{sidepeaks}} = (1 \pm 2\,s)\,f_{\mathrm{s}}. \tag{1}$$

The appearance of large amplitude peaks at $f_{\mathrm{sidepeaks}}$ frequencies is a proven defect symptom. However, to reliably detect such symptoms, the motor must be running under load. Besides, some motor operating conditions lead to masking of side peaks [4]. For example, cyclostationary load, magnetic asymmetry, and axial air ducts in the rotor generate current harmonics in the same frequency range as broken rotor bars. As a result, there is a possibility of false diagnosis and financial loss due to additional maintenance work.

Information on the state of the rotor bars is also contained in the higher-order harmonics of the stator current. A break in the rotor bar leads to the appearance of several peaks in the spectrum of the 5th and 7th harmonics of the stator current [5] (Figure 1). Although the absolute amplitudes of sidebands differ between the 5th and 7th harmonic regions, their relative spectral structure remains consistent. This redundancy enables the use of both harmonics, effectively providing two physically grounded data sources.

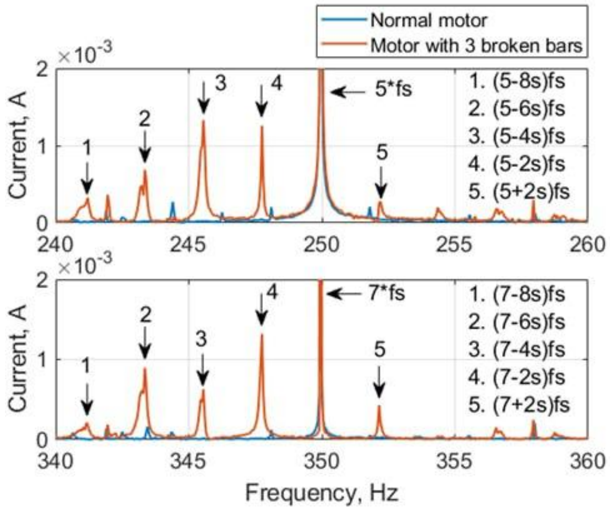

Figure 1. Harmonics of a defect around the 5th and 7th harmonics of the stator current (250 Hz and 350 Hz).

The reason for the appearance of such peaks is related to the magnetomotive force and modulation of the harmonics of the defect by rotation of the rotor relative to the stator [5]. The frequencies of such peaks are calculated using the formulas:

$$f_k = [k\,(1-s) \pm s]\,f_s, \tag{2}$$

where $k = 5, 7, \dots$.

A cyclostationary load can also mask higher order current harmonics. However, in this case its masking effect is lower than in the range of side peaks near the fundamental frequency of the stator current. Thus, analysing the frequency range of the stator current signal in the region of the 5th and 7th harmonics is a more reliable diagnostic approach [6].

This paper proposes a method for diagnosing a rotor bar breakage in an induction motor, based on the analysis of higher harmonics of the stator current signal. Current signals from the motor with and without a defect are received at various motor speeds and load levels. After this, each signal is filtered to extract the useful part of the signal containing the harmonics of the defect. The desired signal is converted into a set of images using the CWT method. Then, the resulting sets are used to train a convolutional neural network. During the training phase, the neural network receives a set of images for one motor speed and one load level. After this, the network is tested on the remaining set. Thus, having a limited set of training data, the model for diagnosing broken rotor bars makes it possible to detect a defect when the motor operating conditions change.

The paper has the following structure: Section 2 reviews related work, Section 3 describes the proposed diagnostic method, Section 4 presents a description of the experiment, Section 5 discusses the results of testing the diagnostic model. The proposed model is trained on data received from the motor at one value of supply frequency and load and tested at other values of frequency and load.

The main contribution of this paper is to show that a diagnostic model developed exclusively for a single operating mode can operate efficiently over a wide range of frequency loads. Therefore, this approach ensures reliable fault detection in industrial environments where it is not possible to collect comprehensive fault data for each operating mode.

2. RELATED WORKS

Most diagnostic methods are based on detecting side harmonics $f_{\mathrm{sidepeaks}}$ in motor currents. One of these methods is the Motor Current Signature Analysis (MCSA) [7]. The MCSA method converts the time signal of the current into a frequency spectrum using the Fourier transform and then estimates the amplitude of the spectrum at side harmonic frequencies. However, according to formulas (1), the harmonics $f_{\mathrm{sidepeaks}}$ depend on the motor slip s, which, in turn, depends on the motor load. When there is no load, the motor slip is minimal, and the harmonics of the rotor defect can merge with the fundamental harmonic of the current. To select defect harmonics in this case, high spectral resolution is required, which leads to long-term collection of signal samples. In addition, the motor must operate in a stationary mode, since changes in the signal lead to blurring of the frequency spectrum. Some modes of motor operation, for example, operation with a frequency converter with vector control, do not provide the necessary stationarity. As a result, the MCSA method can lead to false positives in the diagnostic system [8].

In the problem under consideration, the amplitude of the fundamental power frequency f_{s} is hundreds of times greater than the amplitude of the side frequencies $f_{\mathrm{sidepeaks}}$ and acts as noise that interferes with their determination. Some methods propose to remove the fundamental current harmonic from the signal and thereby simplify the detection of harmonics of a defect [9]. Amplitude demodulation using the Hilbert transform [10], Park's vector approach [11], and the use of the Tiger energy operator (TEO) [12] are similar methods. The Hilbert transform produces an envelope from the current signal containing the ripple associated with the harmonic of the broken bar. Park's vector approach converts a three-phase current system into a two-phase system, resulting in new vector current signals that contain defect information and are less affected by the fundamental current harmonics and noise. The TEO method extracts an energy operator from a single-phase current signal modulated by the harmonic of the defect. It was shown in [13] that all three methods make it possible to obtain a signal containing only harmonics of the rotor defect. The authors of [13] also showed that using the sum of squares of three-phase current signals gives a similar result. In fact, squaring a harmonic signal is also demodulation, where the carrier frequency of the signal is the fundamental frequency of the supply voltage, and the modulating frequency is the frequency of the rotor defect.

Envelope analysis provides more information than analysis of the full current signal. However, there are effects that can mask the harmonics of a defect [8], [14], [15]. Low-frequency load fluctuations, magnetic anisotropy of the rotor core, and the influence of axial air ducts in the rotor can create harmonics in the same frequency range as the rotor defect.

In this regard, some researchers propose to analyse the motor starting currents during start-up [16]-[19]. The characteristic change in the harmonic f_{BB} is clearly visible on the starting current scalograms due to the change in slip s from 1 to the nominal value. This character differs from the effects of cyclostationary loading, which makes it possible to effectively separate defect harmonics and masking effects. However, this approach is not suitable for motors powered by frequency converters. When powered by a frequency converter, the motor slip is kept low during starting. Accordingly, tracking defect symptoms is almost impossible. Also, this approach is not recommended for motors of medium and high power [20], due to the need for frequent shutdowns and starts.

It is shown in [21] that the frequencies $5\ f_s$ and $7\ f$ have much less pronounced amplitude in relation to the side peaks f_k (2) than the frequency f_s in relation to the side peaks $f_{\text{sidepeaks}}$ (1). Thus, the presence of components responsible for the defect is easier to detect by considering the 5th and 7th harmonics [22]. The paper [23] shows that another significant masking effect, magnetic anisotropy of the rotor core, does not affect the current spectrum in the region of the 5th and 7th harmonics. Consequently, detection of a broken rotor bar using higher-order current harmonics is much more promising than analysing the harmonics of the defect in the region of the fundamental frequency of the supply voltage and is chosen in this work.

Existing rotor fault diagnostics primarily rely on two strategies with inherent limitations under variable operation. Methods as MCSA, which analyse sidebands near the fundamental frequency, suffer from masking by its dominant amplitude and require strict stationarity, which is often violated in inverter-fed drives. Start-up transient analysis exploits slip variation during acceleration to separate defect signatures but is inapplicable to motors powered by frequency converters and impractical for medium and high-power machines. Although higher-order harmonics at 5f and 7f have been shown to theoretically reduce masking effects from load variations and magnetic anisotropy, practical implementations capable of robust operation across wide frequency and load variations with limited training data have not been demonstrated yet. The present work addresses this gap by showing that a convolutional neural network trained exclusively on a single operating point achieves robust generalisation across the full operational envelope.

3. PROPOSED METHOD FOR DIAGNOSING ROTOR BAR BREAKAGE

The diagram of the preprocessing stage is shown in Figure 2 and consists of several stages. Preprocessing of stator current signals includes splitting into fragments and filtering with bandwidths $[5\,f-8, 5\,f+8\,]$ and $[7\,f-8, 7\,f+8\,]$ using a Butterworth bandpass filter (normalised steepness 0.97), where f is the supply frequency. Since the motor is powered by a frequency converter operating in scalar mode, the supply frequency remains highly stable with negligible drift. The ±8 Hz passband therefore provides sufficient margin to accommodate minor frequency variations without signal attenuation, eliminating concerns about filter under real operating conditions.

The next step involves training a convolutional neural network model on the resulting set containing images for both the case of a functional motor and the motor with broken bars.

Consider each stage of the method in detail. We use splitting a signal into two-second fragments with 60 % overlap to expand the data set. For each signal fragment, we generate two filtered signals by passing it through filters with bandwidths of $[5\,f-8, 5\,f+8\,]$ and $[7\,f-8, 7\,f+8\,]$. The centre frequencies of the bandpass filters are not fixed but are dynamically set relative to the instantaneous supply frequency of the motor. Figure 3 shows the spectra of the signal envelopes extracted using the Hilbert transform from two filtered current signals for defective and normal cases. They are noticeably similar and have peaks at the same frequencies of $2\,s\,f$, $4\,s\,f$, and $6\,s\,f$, allowing both filtered harmonics to be used to create the data set.

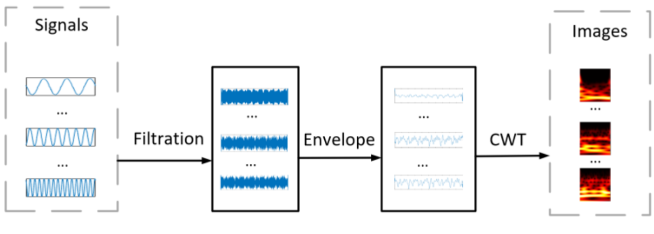

Figure 2. Diagram of the preprocessing stage.

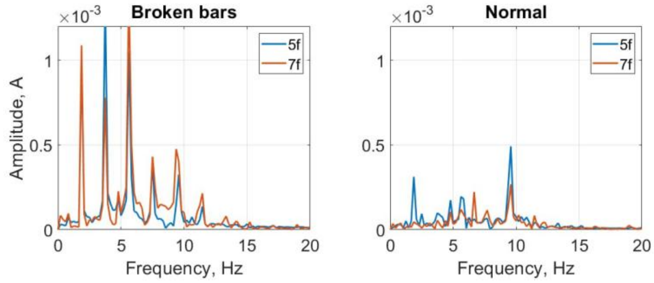

Figure 3. Envelope spectra of harmonics with frequencies in the region of 5f and 7f for a motor with broken bars and a motor with normal bars.

Construction of scalograms uses Matlab functionality. We obtain the coefficients of the continuous wavelet transform by using the built-in CWT function, which provides return values of the function:

$$W_s(a,b)=\frac{1}{\sqrt{a}}\int_{-\infty}^{\infty}s(t)\,\psi\left(\frac{t-b}{a}\right)\mathrm{d}t, \tag{3}$$

where $s(t)$ is the analysed signal, $\psi(t)$ is the mother wavelet, $\psi\left(\frac{t-b}{a}\right)$ are scaled and shifted copies of the mother wavelet, a is the time scale, and b is the time shift.

The graph of the function $W_s(a,b)$ is a surface in three-dimensional space. Matlab constructs its projection onto a plane, the different colors of the points of which correspond to different values of the function $W_s(a,b)$.

We used the mother Morse wavelet, which has proven itself well in the analysis of modulated signals [24]. The symmetry parameter γ was set to 3, and the time bandwidth was set to 60. These values are used in Matlab by default and have shown their optimality in our research. Examples of scalograms corresponding to functional and defective motors are shown in Figure 4 and Figure 5 for supply frequencies of 20 and 40 Hz and load D_0 = 2 % and D_2 = 36 % of the rated torque.

Here the x-axis corresponds to a time period of 2 seconds and the y-axis represents the frequency range from 0 to 20 Hz on a logarithmic scale. The stripes in the figures correspond to the presence of $2\,s\,f$, $4\,s\,f$, and $6\,s\,f$ frequencies in the signals and are in different areas of the images due to different operating conditions of the motor. They also have different brightness depending on the condition of the motor. If there is a broken bar, the stripes are brighter. The difference between normal and defective cases is especially noticeable at high supply frequency and load.

The upper row of Figure 4 and Figure 5 corresponds to the healthy motor condition, while the lower row shows the broken-bar fault condition. A distinct visual difference is observed: scalograms of the healthy condition show substantially lower intensity across the entire time-frequency plane, whereas defect-related sidebands manifest as pronounced horizontal bands in the faulty condition scalograms.

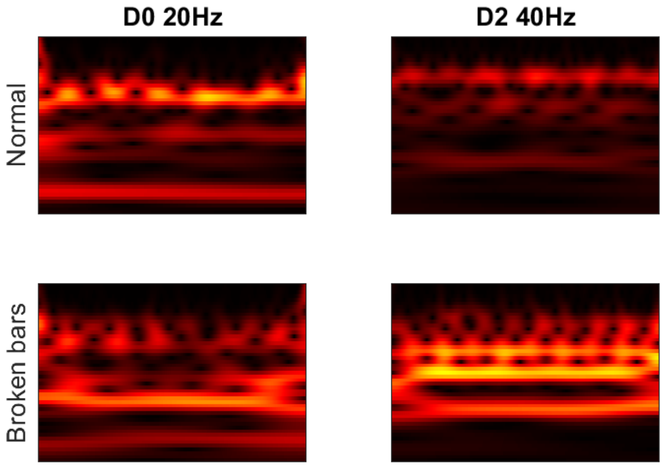

Figure 4. Scalograms corresponding to functional and defective motors under various operating conditions for the $5f$ harmonic.

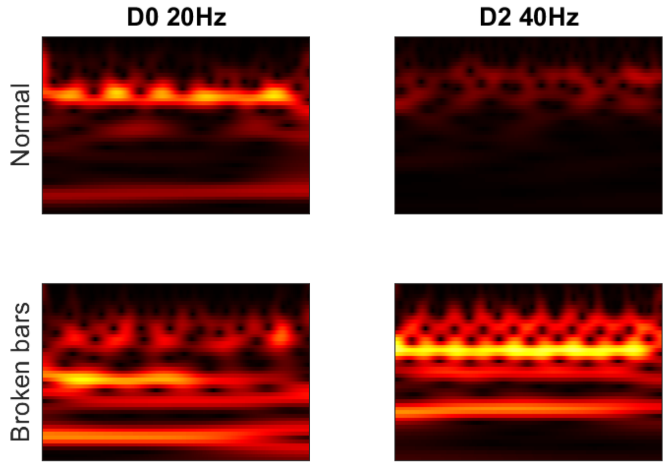

Figure 5. Scalograms corresponding to functional and defective motors under various operating conditions for the $7f$ harmonic.

The bands that sometimes appear in the region of 10-15 Hz are not associated with a defect, but apparently with noise during the operation of the test bench. Their wandering nature contributes to image diversity in the dataset and enhances the model's generalisation capability. Since the 5th and 7th harmonics carry physically redundant information about the same defect mechanism, their scalograms can be fed to the network as independent training samples in parallel, effectively doubling the size of the training dataset.

Next, we use a convolutional neural network model with 9 layers (Figure 6) for training in the created set of images. The first

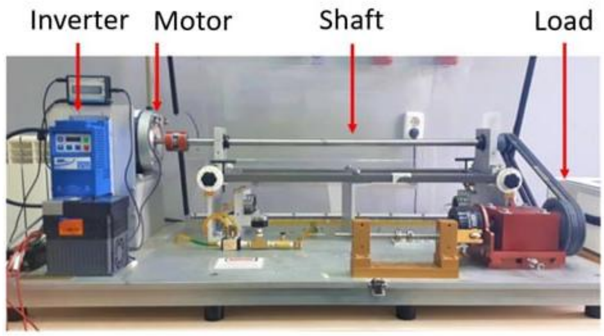

Figure 7. Experimental rig.

Conv2D convolution layer contains 32 kernels for the output of 120×120 feature maps. The next MaxPooling pooling layer outputs 32 pooled maps with a size of 60×60. The second Conv2D convolution layer produces 64 maps with a size of 60×60. The next Maxpooling pooling layer provides 64 30×30 maps. After the third Conv2D convolution layer, there are 128 30×30 maps, which are then stretched into a Dense layer with 2048 neurons. Further, the data is transmitted to two fully connected Dense layers and an output layer of two neurons corresponding to two possible motor conditions (functional/broken).

4. EXPERIMENTAL RIG AND DATA SET

The effectiveness of the proposed diagnostic method was studied based on data obtained on the experimental rig (Figure 7).

The installation consists of an induction motor (IM) with a capacity of 0.37 kW with one pair of poles, a shaft on bearings connected to the motor through a jaw clutch, belt drive, and load. The load is a permanent magnet actuated brake, which sets the torque on the motor shaft. The frequency converter (FC) provides motor power and sets the rotor speed. The parameters of the induction motor are given in Table 1.

Table 1. Motor parameters.

Parameter	Value
Rated power, kW	0.37
Rated voltage, V	220
Rated frequency, Hz	50
Rated torque, N · m	1.24
Number of all rotor bars	34
Number of broken bars	3

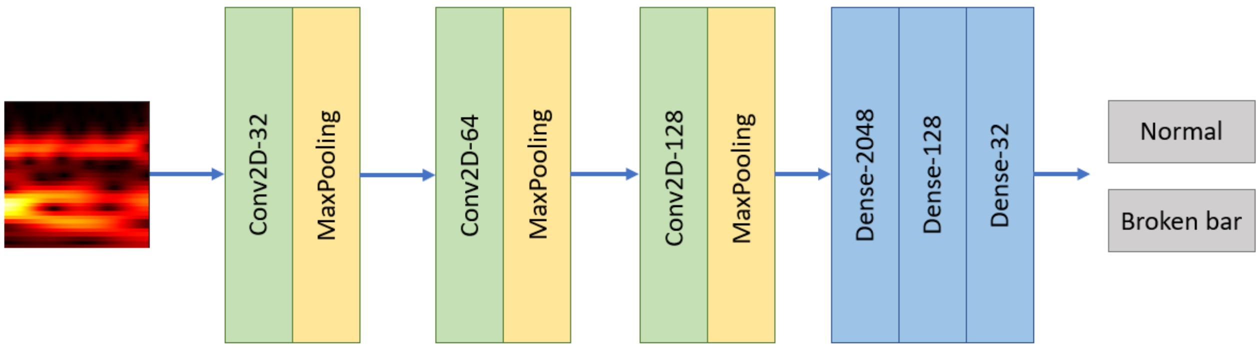

Figure 6. Convolutional neural network model.

The study was conducted for two motors of the same type: a functional motor and a motor with broken rotor bars. The bars were broken by drilling three holes in the region of bars. Stator current was acquired using a Rigol RP1001C (300 kHz bandwidth, two sensitivity ranges: 10 mV/A and 100 mV/A, accuracy ±3 % for currents below 10 A, maximum input ±100 A DC / 200 A AC) connected to a PXI data acquisition system operated via a custom LabVIEW application.

The stator current was measured over the supply voltage frequency range from 10 Hz to 50 Hz with a step of 5 Hz. The experiment was carried out at three levels of load on the motor shaft: D_0 = 2 %, D_1 = 20 %, and D_2 = 36 % of the rated torque. The average slip values for these load levels were 0.024 (D0), 0.030 (D1), and 0.043 (D2). Signals were acquired at a sampling frequency of 50 kHz as continuous 60-second recordings without interruptions. Before each series of measurements, the motor was started operating at rated load to ensure constant winding resistance and eliminate temperature drift of the parameters.

5. RESULTS

5.1. Proposed method

The neural network was trained on scalogram images obtained from pre-processed current signals from a motor with a supply frequency of 25 Hz, under load D_1. The initial training set size was 633 images and was extended to 3133 images using augmentation with an up/down shift of 10 %, which actually corresponded to the frequency shift of $2\,s\,f$, $4\,s\,f$, and $6\,s\,f$ observed when the motor operating conditions changed. Such data set extension contributes to better model performance in unsteady conditions.

The model training used two training control methods: EarlyStopping and ModelCheckpoint callbacks. The first one was responsible for stopping the training of the model. If there was no improvement in accuracy on the validation set for 30 epochs, it stopped training the neural network. The second method retained the best model every time the accuracy improved on the validation set. Thus, after training, the last saved model was taken as the best model. Model training employed the Adam optimizer with a learning rate of 10^{-4}, batch size of 32, and a maximum of 200 epochs. Input scalograms were normalized to the [0, 1] range by dividing pixel intensities by 255. The dataset was split into training and validation subsets using time division, preserving the class balance between healthy and faulty samples. Categorical cross-entropy was taken as a loss function. Figure 8 shows the learning curves. The training was stopped after 100 epochs.

The neural network model trained on the D_1 load and 25 Hz frequency was further tested on the entire dataset. Figure 9 presents the test results. Here, rows D0, D1, and D2 correspond to three load levels. The columns correspond to the power frequency values $f = 10, \dots, 50$ Hz. The table cells present the value of the accuracy metric (proportion of correct answers) of the model for each data set. In cell D1, $f = 25$Hz, corresponding to the motor operating conditions on which the model was trained, its accuracy is 1. Approximately the same accuracy is observed in cells nearby, i.e. with minor changes in frequency and load.

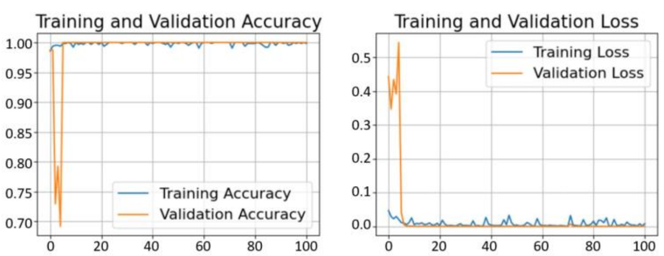

Figure 8. Learning curves.

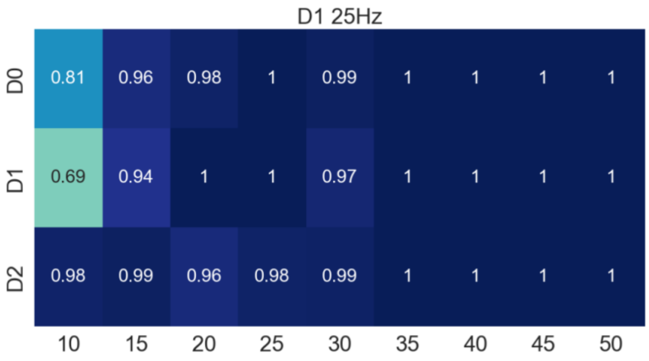

Figure 9. Accuracy of the model trained on data with f = 25 Hz and load D_1.

Figure 10 presents the number of false positive and false negative errors of the model on each data set. The first digit is the number of normal data samples erroneously assigned by the model to defective; the second digit is, on the contrary, the number of defective samples that are incorrectly classified as normal. Note that the test sample contains 400 normal and defective samples in each case.

The model exhibits its lowest accuracy of 0.69 at 10 Hz with D_1 load (20 % torque), with 250 defective samples misclassified as normal (Figure 10). This performance drop has a clear physical explanation: at low supply frequency combined with moderate load, the motor operates with minimal slip, resulting in extremely weak defect-related sidebands that are difficult to distinguish from noise (Figure 11). From an operational perspective, such low-frequency, partial-load regimes represent a narrow operating region often associated with motor idling or transient states. Therefore, this boundary case does not compromise safety-critical diagnostics under normal industrial conditions

For comparison, in the case of a slight increase in the load from $D_1 = 20$ % to $D_2 = 36$ % and the same frequency $f =$ 10 Hz, a significantly better result is 0.98. The spectra corresponding to this case are shown in Figure 12. It can be seen that the defective harmonics have noticeably large amplitude, and the model easily recognizes them.

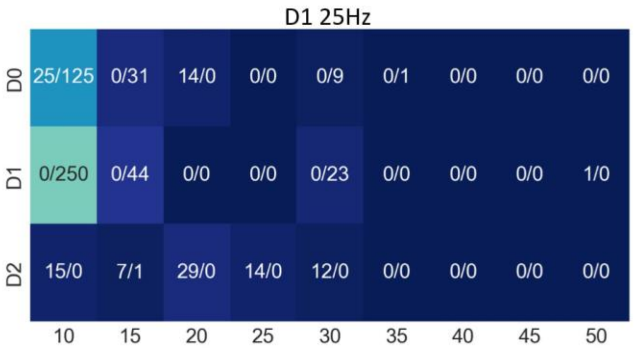

Figure 10. The number of false positive and false negative errors of the model trained on data with f = 25 Hz and load D_1.

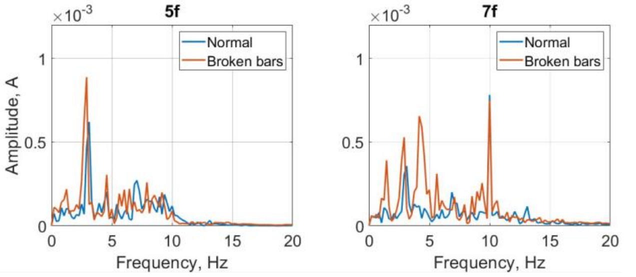

Figure 11. Envelope spectra of the 5th and 7th harmonics for the load D_1 = 20 % and $f = 10$ Hz.

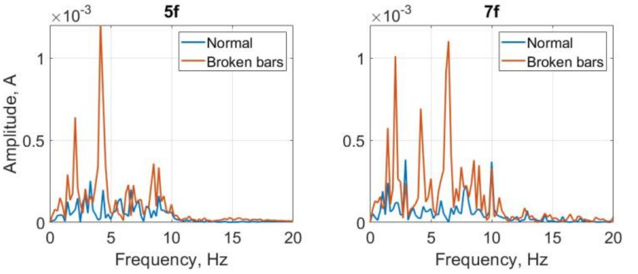

Figure 12. Envelope spectra of the 5th and 7th harmonics for the load D_2 = 36 % and $f = 10$ Hz.

Recall that we trained the model on the central cell, i.e. based on data obtained with load D_1 and a supply frequency of 25 Hz. For comparison, we also trained the model on data with $D_0, f = 25$ Hz. Figure 13 presents the results of testing this model. It can be seen that the accuracy of the model generally degraded. It perfectly classifies samples with similar frequencies and loads located in the neighbourhood of the cell on which the training took place. However, for data with load D_2, the model results are noticeably inferior to those previously observed in Figure 9.

Analysis of the classification error distribution reveals that false positives predominate across most operating conditions: the model tends to misclassify healthy signals as faulty. This error pattern is preferable from an industrial maintenance perspective, as a false alarm from the diagnostic system is less critical than missing an actual fault. However, at low supply frequencies and minimal load levels, the opposite trend emerges – false negatives prevail, with defective signals being erroneously classified as normal. This behaviour is physically explained by the reduced rotor slip under such conditions, which leads to a sharp decrease in the amplitude of informative sidebands in the envelope spectrum and consequently hampers their reliable detection. Nevertheless, the overall proportion of false negative errors remains low, confirming the reliability of the proposed approach for practical industrial deployment.

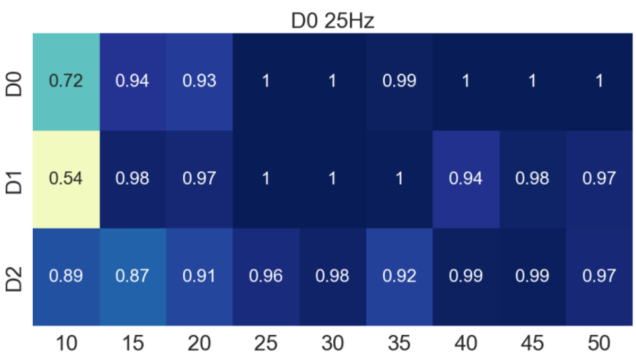

Figure 13. Accuracy of the model trained on data with $f = 25$ Hz and load D_0.

The model achieved an average accuracy of 97 % ± 7 % (mean ± standard deviation) across all 27 test conditions (9 frequencies × 3 load levels). To analyse the results, an F_1 measure was also calculated, calculated as follows:

$$F_1 = 2 \cdot \frac{precision \cdot recall}{precision + recall}, \quad (4)$$

where precision is the ratio of correctly identified faulty images to all images the model classified as faulty, and recall is the ratio of correctly identified faulty images to all actually faulty images in the dataset. The average value F_1 of the model in this case was 0.95.

It should be noted that the reported accuracy is not affected by data leakage despite the overlap between fragments. The train/test split was performed at the level of independent 60-second recordings: the model was trained exclusively on two complete recordings, while testing was conducted on the remaining 52 recordings acquired under different frequency/load conditions. Since no fragment derived from the same 60-second recording appears in both training and testing sets, statistical independence is preserved and the accuracy estimate remains unbiased.

5.2. Alternative approach

For validation of the convolutional architecture choice, a comparative experiment was conducted using a multilayer perceptron trained on automatically extracted numerical features. Feature vectors were generated from the same pre-processed current envelopes, obtained after bandpass filtering around the 5f and 7f supply harmonics followed by Hilbert transform, using the Time Series Feature Extraction Library [25]. This automated procedure yielded 88 temporal, spectral, and statistical features per signal fragment, including statistical moments (mean, variance, skewness, kurtosis), spectral metrics (spectral entropy, median frequency, centroid frequency), cepstral coefficients (LPCC, MFCC), and fractal characteristics.

To enhance robustness against operating condition variations and reduce dimensionality, feature selection was performed using a random forest classifier with 100 trees. Feature importance was evaluated according to the Gini impurity reduction criterion during tree node splitting. Features were retained only if they exceeded the median importance threshold across the ensemble. This selection process yielded a compact 43-dimensional feature vector suitable for efficient classification.

Classification employed a three-layer multilayer perceptron with 32, 16, and 8 neurons in consecutive hidden layers. Each hidden layer utilized ReLU activation, batch normalization, and dropout regularization with a rate of 0.3. Training was performed with the Adam optimizer (learning rate 10^{-4}, batch size 32) and early stopping with a patience of 30 epochs.

When evaluated across the complete test set encompassing all supply frequencies and all three load levels, the multilayer perceptron achieved an average classification accuracy of 70 % ± 15 %. In contrast, the proposed convolutional neural network (Figure 6) operating directly on continuous wavelet transform scalograms attained an average accuracy of 97 %. The 27 % accuracy gap between multilayer perceptron and convolutional neural networks confirms that a simple fully connected model is insufficient. Reliable detection of fault patterns requires an architecture capable of capturing spatial dependencies, precisely the strength of convolutional neural networks.

6. CONCLUSION

This paper presents a data-driven method for broken rotor bar detection in induction motors based on envelope analysis of higher-order stator current harmonics (5f and 7f), continuous wavelet transform for time-frequency image generation, and convolutional neural network classification. The principal contribution lies not in the individual components of the pipeline, which are well established, but in the demonstrated capability of a model trained exclusively on a single operating point (25 Hz supply frequency, 20 % rated torque) to generalise across a wide operational envelope spanning supply frequencies from 10 Hz to 50 Hz and loads from 2 % to 36 % of rated torque. This single-point training paradigm directly addresses a critical industrial constraint: the practical impossibility of collecting labelled fault data under the full spectrum of operating conditions encountered in real-world equipment. The proposed approach achieved an average classification accuracy of 97 % across all tested conditions.

Future work will first address validation across heterogeneous motor populations. Although the present study employed two physically distinct motors of identical type and manufacturing batch. Extending validation to units from different manufacturers and power classes will verify that the model captures universal defect physics rather than signatures tied to a particular motor specimen.

Second, the proposed method will be evaluated on early-stage faults. The current experimental validation used three broken bars to ensure a clear defect signature. Testing the method on motors with one and two broken bars, representing the most common incipient fault conditions, will establish the detection threshold and sensitivity of the approach to milder degradation levels.

REFERENCES

[1] G. K. Singh, Sa'ad Ahmed Saleh Al Kazzaz, Induction machine drive condition monitoring and diagnostic research – a survey, Electric Power Systems Research, 2003, vol. 64, no. 2, pp. 145-158.
DOI: 10.1016/S0378-7796(02)00172-4

[2] M. Garcia, A. Panagiotou, Efficiency Assessment of Induction Motors Operating Under Different Faulty Conditions, IEEE Transactions on Industrial Electronics, 2019, vol. 66, no. 10, pp. 8072-8081.
DOI: 10.1109/TIE.2018.2885719

[3] S. B. Lee, G. C. Stone, J. Antonino-Daviu, K. N. Gyftakis, E. G. Strangas, P. Maussion, C. A. Platero, Condition monitoring of industrial electric machines: state of the art and future challenges, IEEE Industrial Electronics Magazine, 2020, vol. 12, pp. 158-167.
DOI: 10.1109/MIE.2020.3016138

[4] M. J. Lighthill, Contribution to the theory of heat transfer through a laminar boundary layer, Proc. of Roy. Soc., London, 1950, A 202, pp. 359-377. Online [Accessed 25 August 2026]
https://www.jstor.org/stable/98524

[5] J. Tang, Y. Yang, J. Chen, R. Qiu., Z. Liu, Characteristics Analysis and Measurement of Inverter-Fed Induction Motors for Stator and Rotor Fault Detection, Energies, 2020, vol. 13, no. 1, p. 101.
DOI: 10.3390/en13010101

[6] P. A. Panagiotou, J. C. Mayo-Maldonado, I. Arvanitakis, G. Escobar, J. A. Antonino-Daviu, K. N. Gyftakis, A Novel Method for Rotor Fault Diagnostics in Induction Motors using Harmonic Isolation, 2023 IEEE 14th Int. Symp. on Diagnostics for Electrical Machines, Power Electronics and Drives (SDEMPED), Chania, Greece, 2023, pp. 265-271.
DOI: 10.1109/SDEMPED54949.2023.10271499

[7] G. B. Kliman, J. Stein, Methods of Motor Current Signature Analysis, Electr. Mach. Power Syst., vol. 20, no. 5, Sep. 1992, pp. 463–474.
DOI: 10.1080/07313569208909609

[8] S. Bin Lee, Identification of False Rotor Fault Indications Produced by Online MCSA for Medium-Voltage Induction Machines, IEEE Trans. Ind. Appl., vol. 52, no. 1, Jan. 2016, pp. 729–739.
DOI: 10.1109/TIA.2015.2464301

[9] A. Shestakov, O. Ibryaeva, V. Eremeeva, V. Sinitsin, The Detection of Rotor Bar Faults Using Recursive Matrix Pencil Method, 19th IMEKO TC10 Conference "MACRO meets NANO in Measurement for Diagnostics, Optimization and Control", Delft, The Netherlands, 21-23 September 2023, 6 pp.
DOI: 10.21014/tc10-2023.015

[10] M. B. Abd-el-Malek, A. K. Abdelsalam, O. E. Hassan, Novel approach using Hilbert Transform for multiple broken rotor bars fault location detection for three phase induction motor, ISA Trans., vol. 80, Sep. 2018, pp. 439–457.
DOI: 10.1016/j.isatra.2018.07.020

[11] K. N. Gyftakis, A. J. Marques Cardoso, J. A. Antonino-Daviu, Introducing the Filtered Park's and Filtered Extended Park's Vector Approach to detect broken rotor bars in induction motors independently from the rotor slots number, Mech. Syst. Signal Process., vol. 93, Sep. 2017, pp. 30–50.
DOI: 10.1016/j.ymssp.2017.01.046

[12] H. Li, W. Zuolu, D. Zhen, F. Gu, A. Ball, Modulation Sideband Separation Using the Teager–Kaiser Energy Operator for Rotor Fault Diagnostics of Induction Motors, Energies, vol. 12, no. 23, Nov. 2019, p. 4437.
DOI: 10.3390/en12234437

[13] J. Chen, N. Hu, L. Zhang, L. Chen, B. Wang, Y. Zhou, A Method for Broken Rotor Bars Diagnosis Based on Sum-Of-Squares of Current Signals, Appl. Sci., vol. 10, no. 17, Aug. 2020, p. 5980.
DOI: 10.3390/app10175980

[14] M. E. H. Benbouzid, G. B. Kliman, What stator current processing-based technique to use for induction motor rotor faults diagnosis? IEEE Trans. Energy Convers., vol. 18, no. 2, Jun. 2003, pp. 238–244.
DOI: 10.1109/TEC.2003.811741

[15] J. Kim, S. Shin, S. Bin Lee, K. N. Gyftakis, M. Drif, A. J. M. Cardoso, Power Spectrum-Based Detection of Induction Motor Rotor Faults for Immunity to False Alarms, IEEE Trans. Energy Convers., vol. 30, no. 3, Sep. 2015, pp. 1123–1132.
DOI: 10.1109/TEC.2015.2423315

[16] J. A. Antonino-Daviu, M. Riera-Guasp, J. R. Folch, M. P. M. Palomares, Validation of a new method for the diagnosis of rotor bar failures via wavelet transform in industrial induction machines, IEEE Trans. Ind. Appl., vol. 42, no. 4, Jul. 2006, pp. 990–996.
DOI: 10.1109/TIA.2006.876082

[17] C. Yang., Starting Current Analysis in Medium Voltage Induction Motors: Detecting Rotor Faults and Reactor Starting Defects, IEEE Ind. Appl. Mag., vol. 25, no. 6, Nov. 2019, pp. 69–79.
DOI: 10.1109/MIAS.2019.2923105

[18] J. A. Antonino-Daviu, J. Pons-Llinares, S. Bin Lee, Advanced Rotor Fault Diagnosis for Medium-Voltage Induction Motors Via Continuous Transforms, IEEE Trans. Ind. Appl., vol. 52, no. 5, Sep. 2016, pp. 4503–4509.
DOI: 10.1109/TIA.2016.2582720

[19] S. B. Lee, D. Hyun, T.-J. Kang, C. Yang, S. Shin, H. Kim, S. Park, T.-S. Kong, H.-D. Kim, Identification of false rotor fault indications produced by online MCSA for medium-voltage induction machines, IEEE Transactions on Industry Applications. 2016. vol. 52, no. 1, pp. 729-739.
DOI: 10.1109/TIA.2015.2464301

[20] P. Zhang, Y. Du, T. G. Habetler, B. Lu, A Survey of Condition Monitoring and Protection Methods for Medium-Voltage Induction Motors, IEEE Transactions on Industry Applications. 2011, vol. 47, no. 1, pp. 34-46.
DOI: 10.1109/TIA.2010.2090839

[21] H. Kim, S. Bin Lee, S. Park, S. H. Kia, G.-A. Capolino, Reliable Detection of Rotor Faults Under the Influence of Low-Frequency Load Torque Oscillations for Applications with Speed Reduction Couplings, IEEE Trans. Ind. Appl., vol. 52, no. 2, Mar. 2016, pp. 1460–1468.
DOI: 10.1109/TIA.2015.2508423

[22] A. Shestakov, O. Ibryaeva, V. Eremeeva, V. Sinitsin, Detection of Broken Bar Fault in Induction Motor Using Higher-Order Harmonics Analysis, 19th IMEKO TC10 Conference "MACRO meets NANO in Measurement for Diagnostics, Optimization and Control", Delft, The Netherlands, 21-23 September 2023, 6 pp.
DOI: 10.21014/tc10-2023.010

[23] S. Shin, J. Kim, S. Bin Lee, C. Lim, E. J. Wiedenbrug, Evaluation of the influence of rotor magnetic anisotropy on condition monitoring of 2 pole induction motors, in 2014 IEEE Energy Conversion Congress and Exposition (ECCE), IEEE, Sep. 2014, pp. 638–645.
DOI: 10.1109/TIA.2015.2391432

[24] J. M. Lilly, S. C. Olhede, Generalized Morse wavelets as a superfamily of analytic wavelets, IEEE Transactions on Signal Processing Vol. 60, No. 11, 2012, pp. 6036-6041.
DOI: 10.1109/TSP.2012.2210890

[25] M. Barandas, D. Folgado, L. Fernandes, S. Santos, M. Abreu, P. Bota, H. Liu, T. Schultz, H. Gamboa, TSFEL: Time Series Feature Extraction Library, SoftwareX 2020, 11, 100456.
DOI: 10.1016/j.softx.2020.100456